The Flow through the Gulf of Mexico

J. Candela, J. Ochoa, J. Sheinbaum, M. López, P. Pérez-Brunius,
M. Tenreiro, and E. Pallàs-Sanz

Departamento de Oceanografía Física, CICESE, Ensenada, Baja California, Mexico

G. Athié

Cátedra CONACYT–ICIMAP, Universidad Veracruzana, Xalapa, Veracruz, Mexico

L. Arriaza-Oliveros

ICIMAR, Havana, Cuba

(Manuscript received 22 September 2018, in final form 13 March 2019)

ABSTRACT

Four years (September 2012 to August 2016) of simultaneous current observations across the Yucatan Channel (~21.5°N) and the Straits of Florida (~81°W) have permitted us to investigate the characteristics of the flow through the Gulf of Mexico. The average transport in both channels is 27.6 Sv (1 Sv = 10^6 m^3 s^{-1}), in accordance with previous estimates. At the Straits of Florida section, the transport related to the astronomical tide explains 55% of the observed variance with a mixed semidiurnal/diurnal character, while in the Yucatan Channel tides contribute 82% of the total variance and present a dominant diurnal character. At periods longer than a week the transports in the Yucatan and Florida sections have a correlation of 0.83 without any appreciable lag. The yearly running means of the transport time series in both channels are well correlated (0.98) and present a 3-Sv range variation in the 4 years analyzed. This long-term variability is well related to the convergence of the Sverdrup transport in the North Atlantic between 14.25° and 18.75°N. Using 2 years (July 2014–July 2016) of simultaneous currents observations in the Florida section, the Florida Cable section (~26.7°N), and a section across the Old Bahama Channel (~78.4°W), a mean northward transport of 28.4, 31.1, and 1.6 Sv, respectively, is obtained, implying that only 1.1 Sv is contributed by the Northwest Providence Channel to the mean transport observed at the Cable section during this 2-yr period.

1. Introduction

The flow through the Gulf of Mexico (GoM) is an integral part of the North Atlantic subtropical gyre circulation. According to Schmitz and McCartney (1993), the long-term mean flow between Florida and the Bahamas at the Cable section (~26.7°N) amounts to 31 Sv (1 Sv = 10^6 m^3 s^{-1}) and is composed of roughly equal parts by the compensation of the Sverdrup transport due to the wind stress curl over the North Atlantic and to the upper branch of the global meridional overturning cell (MOC), which compensates the export of North Atlantic Deep Water (NADW) to the southern Atlantic. This work reports, for the first time, simultaneous current measurements across the Yucatan Channel and on a section in the Florida Straits at ~81°W for a period of 4 years (September 2012–August 2016). Contrary to what is measured at the Florida Cable, this section only considers flows through the GoM, without inputs from the Old Bahama or the Northwest Providence Channels, which, as shown later, even though contributing just a few Sverdrups to the mean flow, can add important variability to the observed flow (Fig. 1). Therefore, the flow measured through this section at ~81°W is a more accurate indicator of the Loop Current flow out of the GoM than what is measured at the Florida Cable, as noted earlier by Hamilton et al. (2005).

ⓓ Denotes content that is immediately available upon publication as open access.

🔗 Supplemental information related to this paper is available at the Journals Online website: https://doi.org/10.1175/JPO-D-18-0189.s1.

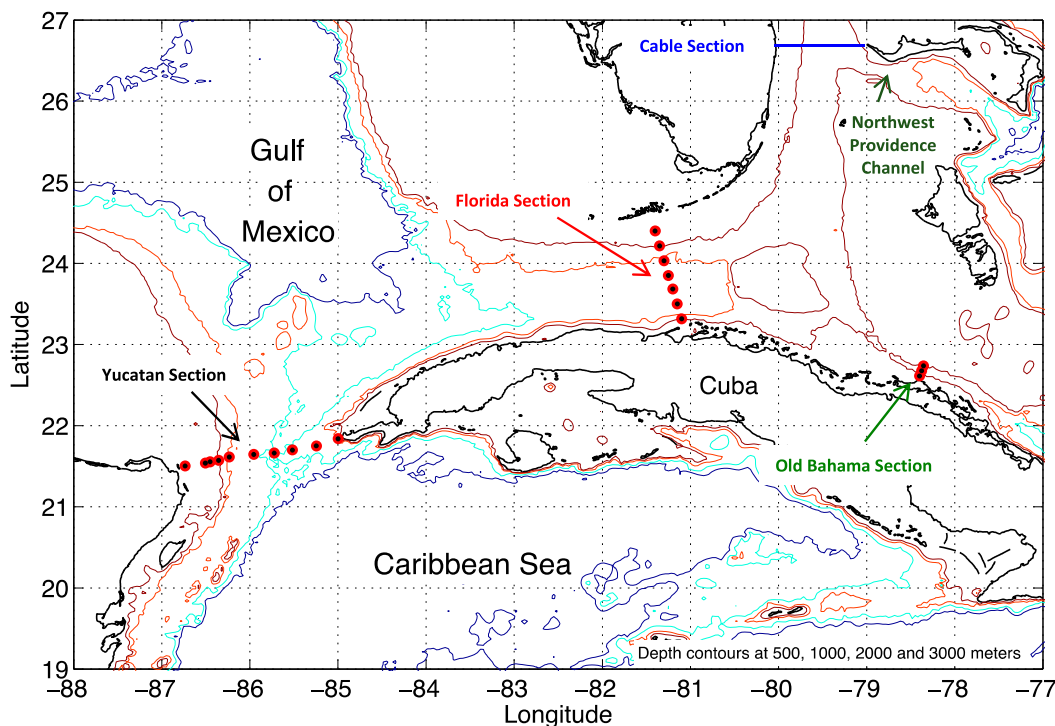*Corresponding author*: Julio Candela, jcandela@cicese.mx

FIG. 1. Location of moorings in the Yucatan Channel, Florida Straits, and Old Bahama Channel sections.

The motivation for simultaneously measuring the Yucatan and Florida sections was twofold. First, it was realized that controlling the entrance and exit of the GoM throughflow would shed light for understanding important features of the GoM dynamics and particularly of the Loop Current behavior, a subject not to be addressed in this article. Second, previous efforts to measure the current structure and transport in the Yucatan Channel (Sheinbaum et al. 2002; Abascal et al. 2003; Ochoa et al. 2003; Athié et al. 2015) had revealed a very variable and complex channel, both oceanographically and bathymetrically, that was complicated to measure and therefore it would be convenient to have some independent measurement to verify at least its total transport. Considering the surface area of the GoM ($\sim 1.6 \times 10^{12}\,\mathrm{m}^2$), a 1-Sv imbalance between Yucatan and Florida transports for a day would imply a $\sim$5-cm sea level change within the GoM, therefore the total transports between the two sections have to coincide quite strictly in periods longer than a few days. Since the western Florida Straits, between the Florida Keys and Cuba, has a more regular and simple cross section, measuring the transport there seemed to be a good option to obtain an independent estimate of total transport to compare with that obtained in Yucatan.

The first effort made to measure the transport through Yucatan Channel from continuous current series was carried out between 1999 and 2001, with a 21-month average transport of 22.8 ± 0.3 Sv (Sheinbaum et al. 2002; Ochoa et al. 2003). Further studies with a similar mooring array, but with more instruments and two additional moorings, reported a transport of 26.1 ± 0.5 Sv from 23 months of velocity measurements (Athié et al. 2015; 27.1 Sv between May 2010 and May 2011 and 25.0 Sv between July 2012 and June 2013). Both the anomalous low transport values measured in 1999–2001 and these latter larger transport values obtained in 2010–13 were well correlated with a transport proxy based on 20 years of altimetry data (Athié et al. 2015). In particular, the low transport values during 1999–2001 were consistent with quite anomalous geostrophic velocities from altimetry in the Yucatan, Florida, and Old Bahama Channels. These authors suggested that significant compensation through other channels off the GoM was required to match the 32-Sv mean transport from cable measurements of the Florida Current at 27°N (Meinen et al. 2010), as also suggested in the work of Hamilton et al. (2005). In that regard, our measurements in the Old Bahama Channel discussed below in section 4 corroborate the relevance of that flow to understand the variability of the Florida Current and the plausibility of substantial transports even if the mean is small, in contrast to suggestions of the contrary (Rousset and Beal 2011).
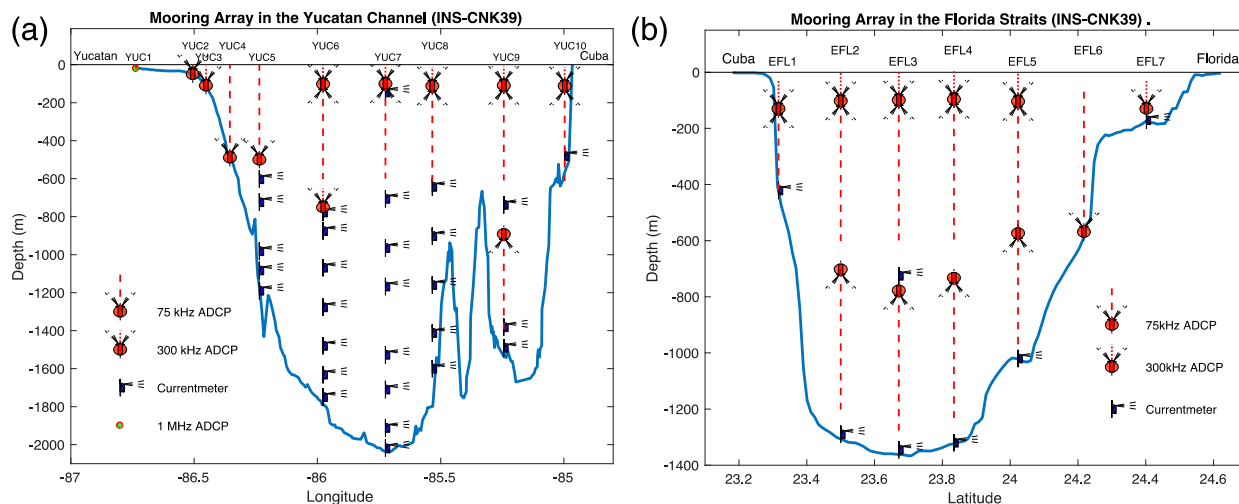
FIG. 2. (a) Instruments in the Yucatan mooring array. The labels on top indicate the name of the mooring. Dashed or dotted lines on the ADCPs indicate their nominal profiling range which for the 300-kHz ADCP is 100 m and for the 75-kHz ADCP is 500 m. The 1-MHz ADCP at YUC1 profiles 20 m. (b) Instruments in the Florida Straits mooring array. The labels on top indicate the name of the mooring. Dashed or dotted lines on the ADCPs indicate their nominal profiling range which for the 300-kHz ADCP is 100 m and for the 75-kHz ADCP is 500 m.

In the next section the mooring observations are described along with the transport interpolation method used. Section 3 reports the transport estimates and their relation to the Sverdrup transport, calculated using the ERA-Interim wind product (Berrisford et al. 2011) in the North Atlantic. Section 4 relates estimates of transport at the Cable section and at the Old Bahama Channel, both outside the GoM, with two years of simultaneous measurements at the Florida section. The implications of the results are discussed in section 5 followed by some concluding remarks.

2. Data and methods

Ten moorings across the Yucatan Channel and seven moorings across the Florida Straits section were initially installed in the summer of 2012 and maintained until the summer of 2016, with yearly services during the summers of 2013, 2014, and 2015. Each mooring in the two sections, that is, Yucatan and Florida, were designed to measure current in the whole water column with a suite of acoustic Doppler current profilers (ADCPs) and single-level current meters (see Figs. 2a,b). All instruments, ADCPs and point current meters, also recorded temperature measurements. Most ADCPs and current meters measured pressure in order to monitor the instantaneous depth of each instrument on the mooring. The nominal sampling depth, time, and parameters measured by each instrument in the mooring deployments are indicated in Tables 1 and 2. Independent of the initial sampling time of each instrument,

all data series used were resampled to hourly values. Figure 2a corresponds to the fourth deployment in Yucatan (CNK39) and had 28 point measuring current meters distributed in the deep part of moorings YUC5 to YUC9. The previous three deployments had about half as many deep current meters in these moorings with 11 in CNK29, 11 in Cnk34, and 15 in CNK37 (see Table 1). As discussed later, this thinner instrument coverage in the deep part of the Yucatan section during the first three deployments had important consequences on the reconstruction of the transport time series. In the case of the Florida section all four deployments had equivalent amounts of instrumentation, and a reasonable coverage of the section was obtained in all four deployments (Fig. 2b, Table 2).

Transport interpolation method

A basic optimal estimation method (Bretherton et al. 1976; Roemmich 1983) with iterations is used to interpolate the current structure in each section. The iteration procedure is implemented to determine the most appropriate reference mean field, being aware that the objective interpolation is most suitable for anomalies. The procedure is as follows: a set of horizontal and vertical scales is chosen for objectively interpolating the hourly current maps in the channel section. Initially, an arbitrary mean current is chosen as the mean reference field (this can be a zero current map or any other appropriate mean field). At each hourly time step, the available current anomaly observations in the channel's section are determined considering their instantaneous

TABLE 1. Characteristics of the moorings deployed across Yucatan Channel in the four deployments (CNK29, CNK34, CNK37 and CNK39) described in the text. The instruments names correspond to: AQP, 1-MHz ADCP; WH300, 300-kHz ADCP; LR, 75-kHz ADCP; A2L, A3L, A6L, NORTEK AQU/ADOP single-point acoustic current meters with corresponding 2000-, 3000-, and 6000-m depth rating. AaRCM11 and AaSg: AANDERAA single-point Doppler recording current meters, models RCM 11 and SEAGUARD, respectively. SBE56: SEABIRD Electronics temperature sensor. The UP or DW suffix indicates corresponding upward or downward orientation of the ADCPs.

Mooring	Latitude	Longitude	Water depth (m)	Instrument	Instrument depth (m)	Start	End	Length of series (days)	No. of bins	Bin size (m)
						Recovery Cruise CNK29				
YUC1	21°30.228'N	86°44.137'W	21	AQPUP	20	1600 UTC 30 Jun 2012	2200 UTC 18 Jun 2013	353	16	1
YUC2	21°32.312'N	86°30.341'W	63	WH300UP	50	0200 UTC 30 Jun 2012	2200 UTC 22 Mar 2013	265	10	4
YUC3	21°33.244'N	86°27.050'W	118	WH300UP	110	0200 UTC 30 Jun 2012	2100 UTC 17 Jun 2013	352	11	8
YUC4	21°34.227'N	86°21.319'W	499	LR75UP	490	0000 UTC 30 Jun 2012	2000 UTC 17 Jun 2013	352	27	16
YUC5	21°36.082'N	86°13.787'W	1260	LR75UP	497	1400 UTC 29 Jun 2012	1700 UTC 17 Jun 2013	353	31	16
				A2L	722	1500 UTC 29 Jun 2012	1800 UTC 17 Jun 2013	353		
				A3L	1080	1500 UTC 29 Jun 2012	1800 UTC 17 Jun 2013	353		
YUC6	21°39.855'N	85°59.106'W	1890	LR75UP	500	0000 UTC 29 Jun 2012	2000 UTC 16 Jun 2013	352	27	16
				WH300DW	500	2200 UTC 28 Jun 2012	1900 UTC 16 Jun 2013	352	12	8
				WH300UP	762	2200 UTC 28 Jun 2012	2000 UTC 16 Jun 2013	352	11	8
				A2L	871	0000 UTC 29 Jun 2012	2000 UTC 16 Jun 2013	352		
				A2L	1280	0000 UTC 29 Jun 2012	1900 UTC 16 Jun 2013	352		
				A3L	1583	0000 UTC 29 Jun 2012	2000 UTC 16 Jun 2013	352		
YUC7	21°39.406'N	85°42.491'W	2041	LR75UP	509	2000 UTC 28 Jun 2012	0900 UTC 17 Jun 2013	353	27	16
				WH300DW	509	2000 UTC 28 Jun 2012	0900 UTC 17 Jun 2013	353	10	8
				A2L	711	2100 UTC 28 Jun 2012	0800 UTC 17 Jun 2013	353		
				A6L	1170	2100 UTC 28 Jun 2012	0800 UTC 17 Jun 2013	353		
				A6L	1910	2100 UTC 28 Jun 2012	0800 UTC 17 Jun 2013	353		
YUC8	21°41.241'N	85°31.115'W	1693	LR75DW	126	1900 UTC 05 Jul 2012	1100 UTC 24 Jun 2013	353	36	16
				A3L	651	2000 UTC 05 Jul 2012	1100 UTC 24 Jun 2013	353		
				A3L	1159	2000 UTC 05 Jul 2012	1100 UTC 24 Jun 2013	353		
YUC9	21°44.348'N	85°17.793'W	1536	LR75DW	142	2100 UTC 05 Jul 2012	1300 UTC 24 Jun 2013	353	34	16
				WH300UP	142	2200 UTC 05 Jul 2012	1300 UTC 24 Jun 2013	353	14	8
				A3L	745	2100 UTC 05 Jul 2012	1400 UTC 24 Jun 2013	353		
				LR75DW	1097	2200 UTC 05 Jul 2012	1300 UTC 24 Jun 2013	353	13	16
YUC10	21°48.071'N	84°58.513'W	641	LR75DW	127	0200 UTC 06 Jul 2012	1400 UTC 07 Aug 2012	32	25	16
				WH300UP	127	0300 UTC 06 Jul 2012	1800 UTC 24 Jun 2013	353	11	8
						Recovery Cruise CNK34				
YUC1	21°30.228'N	86°44.137'W	21	AQPUP	20	0000 UTC 23 Jun 2013	1700 UTC 02 Jul 2014	374	16	1
YUC2	21°32.354'N	86°30.326'W	61	WH300UP	50	0200 UTC 19 Jun 2013	1100 UTC 02 Jul 2014	378	10	4
YUC3	21°33.265'N	86°27.112'W	115	WH300UP	107	0300 UTC 19 Jun 2013	1000 UTC 02 Jul 2014	378	11	8
YUC4	21°34.256'N	86°21.316'W	504	LR75UP	490	2100 UTC 18 Jun 2013	0900 UTC 02 Jul 2014	378	44	10
YUC5	21°36.740'N	86°14.224'W	1156	LR75UP	496	1300 UTC 18 Jun 2013	2000 UTC 01 Jul 2014	378	40	10
				A2L	599	1500 UTC 18 Jun 2013	2100 UTC 01 Jul 2014	378		
				A3L	978	1500 UTC 18 Jun 2013	2100 UTC 01 Jul 2014	378		

TABLE 1. (*Continued*)

Mooring	Latitude	Longitude	Water depth (m)	Instrument	Instrument depth (m)	Start	End	Length of series (days)	No. of bins	Bin size (m)
YUC6	21°40.098'N	85°58.761'W	1883	A6L	1148	1400 UTC 18 Jun 2013	2100 UTC 01 Jul 2014	378		
				LR75DW	108	1800 UTC 17 Jun 2013	1400 UTC 01 Jul 2014	378	36	16
				WH300UP	108	1800 UTC 17 Jun 2013	1500 UTC 01 Jul 2014	378	10	8
				A3L	765	1800 UTC 17 Jun 2013	1400 UTC 01 Jul 2014	378		
				WH300UP	763	1900 UTC 17 Jun 2013	1500 UTC 01 Jul 2014	378	14	8
				A3L	1074	1900 UTC 17 Jun 2013	1500 UTC 01 Jul 2014	378		
				A6L	1583	1900 UTC 17 Jun 2013	1500 UTC 01 Jul 2014	378		
YUC7	21°39.331'N	85°43.438'W	2038	LR75DW	107	1500 UTC 17 Jun 2013	1000 UTC 01 Jul 2014	378	36	16
				A2L	711	1500 UTC 17 Jun 2013	0900 UTC 01 Jul 2014	378		
				A2L	1528	1500 UTC 17 Jun 2013	1000 UTC 01 Jul 2014	378		
YUC8	21°41.901'N	85°31.009'W	1700	LR75DW	126	0300 UTC 25 Jun 2013	1600 UTC 08 Feb 2014	228	36	16
				WH300UP	126	0300 UTC 25 Jun 2013	0900 UTC 08 Jul 2014	378	15	8
				A2L	651	0400 UTC 25 Jun 2013	0900 UTC 08 Jul 2014	378		
				A6L	905	0400 UTC 25 Jun 2013	1000 UTC 08 Jul 2014	378		
YUC9	21°44.531'N	85°17.753'W	1504	LR75DW	142	1300 UTC 25 Jun 2013	1100 UTC 08 Jul 2014	377	36	16
				A3L	745	1300 UTC 25 Jun 2013	1100 UTC 08 Jul 2014	377		
				LR75DW	1097	1400 UTC 25 Jun 2013	1200 UTC 08 Jul 2014	377	18	16
YUC10	21°48.073'N	84°58.501'W	632	LR75DW	127	1500 UTC 25 Jun 2013	1900 UTC 13 Jul 2014	383	25	16
				WH300UP	127	1500 UTC 25 Jun 2013	1900 UTC 13 Jul 2014	383	16	8
Recovery Cruise CNK37										
YUC1	21°30.228'N	86°44.137'W	21	AQPUP	20	1900 UTC 02 Jul 2014	1300 UTC 01 Jun 2015	333	16	1
YUC2	21°32.359'N	86°30.327'W	60	WH300UP	50	1600 UTC 02 Jul 2014	1300 UTC 07 Jul 2015	369	10	4
YUC3	21°33.270'N	86°27.102'W	115	WH300UP	107	2000 UTC 02 Jul 2014	1200 UTC 07 Jul 2015	369	10	8
YUC4	21°34.267'N	86°21.325'W	504	LR75UP	490	2100 UTC 06 Jul 2014	1000 UTC 07 Jul 2015	365	53	8
YUC5	21°36.826'N	86°14.234'W	1138	LR75UP	498	0300 UTC 02 Jul 2014	2200 UTC 06 Jul 2015	369	47	8
				SBE56	601	0300 UTC 02 Jul 2014	0300 UTC 01 Aug 2014	216		
				A2L	723	0300 UTC 02 Jul 2014	2200 UTC 06 Jul 2015	369		
				SBE56	723	0300 UTC 02 Jul 2014	2300 UTC 06 Jul 2015	30		
				A3L	1082	0500 UTC 02 Jul 2014	1600 UTC 03 Feb 2015	369		
				SBE56	1082	0500 UTC 02 Jul 2014	2100 UTC 06 Jul 2015	369		
				A3L	1130	0500 UTC 02 Jul 2014	2100 UTC 06 Jul 2015	369		
YUC6	21°40.041'N	85°58.635'W	1871	LR75DW	107	2200 UTC 01 Jul 2014	1700 UTC 06 Jul 2015	369	35	16
				WH300UP	107	2200 UTC 01 Jul 2014	1700 UTC 06 Jul 2015	369	9	8
				SBE56	107	2200 UTC 01 Jul 2014	1800 UTC 06 Jul 2015	369		
				WH300UP	761	2200 UTC 01 Jul 2014	1800 UTC 06 Jul 2015	369	10	8
				SBE56	763	2200 UTC 01 Jul 2014	1800 UTC 06 Jul 2015	369		
				A2L	870	0000 UTC 02 Jul 2014	1600 UTC 06 Jul 2015	369		
				SBE56	1071	0000 UTC 02 Jul 2014	1600 UTC 06 Jul 2015	369		
				A3L	1278	0000 UTC 02 Jul 2014	1600 UTC 06 Jul 2015	369		
				SBE56	1278	0000 UTC 02 Jul 2014	1600 UTC 06 Jul 2015	369		

TABLE 1. (Continued)

Mooring	Latitude	Longitude	Water depth (m)	Instrument	Instrument depth (m)	Start	End	Length of series (days)	No. of bins	Bin size (m)
YUC7	21°39.581′N	85°43.446′W	2026	LR75DW	109	1600 UTC 01 Jul 2014	1300 UTC 06 Jul 2015	369	35	16
				WH300UP	109	1600 UTC 01 Jul 2014	1100 UTC 06 Jul 2015	369	11	8
				SBE56	109	1600 UTC 01 Jul 2014	1300 UTC 06 Jul 2015	369		
				A2L	713	1600 UTC 01 Jul 2014	1300 UTC 06 Jul 2015	369		
				SBE56	713	1600 UTC 01 Jul 2014	1300 UTC 06 Jul 2015	369		
				SBE56	970	1600 UTC 01 Jul 2014	1300 UTC 06 Jul 2015	369		
				A3L	1172	1800 UTC 01 Jul 2014	1100 UTC 06 Jul 2015	369		
				SBE56	1172	1800 UTC 01 Jul 2014	1100 UTC 06 Jul 2015	369		
				A3L	1529	1800 UTC 01 Jul 2014	1100 UTC 06 Jul 2015	369		
				A3L	1912	1800 UTC 01 Jul 2014	1100 UTC 06 Jul 2015	369		
YUC8	21°42.129′N	85°31.121′W	1689	LR75DW	126	0400 UTC 09 Jul 2014	1000 UTC 06 Jul 2015	362	34	16
				WH300UP	126	0400 UTC 09 Jul 2014	0900 UTC 06 Jul 2015	362	14	8
				AaRCM11	652	0400 UTC 09 Jul 2014	0600 UTC 08 Sep 2014	362		
				SBE56	652	0300 UTC 09 Jul 2014	1100 UTC 06 Jul 2015	362		
				SBE56	906	0700 UTC 09 Jul 2014	1100 UTC 06 Jul 2015	362		
				AaRCM11	1160	0600 UTC 09 Jul 2014	0800 UTC 06 Jul 2015	362		
				SBE56	1160	0600 UTC 09 Jul 2014	0800 UTC 06 Jul 2015	362		
				A3L	1412	0600 UTC 09 Jul 2014	0800 UTC 06 Jul 2015	61		
YUC9	21°44.947′N	85°14.652′W	1804	LR75DW	142	0700 UTC 09 Jul 2014	1300 UTC 09 Jul 2015	365	35	16
				WH300UP	142	0600 UTC 09 Jul 2014	1300 UTC 09 Jul 2015	365	15	8
				AaRCM11	745	0600 UTC 09 Jul 2014	1300 UTC 09 Jul 2015	365		
				SBE56	745	0700 UTC 09 Jul 2014	1300 UTC 09 Jul 2015	365		
				LR75DW	1097	0700 UTC 09 Jul 2014	1300 UTC 09 Jul 2015	365	16	16
				A3L	1582	0700 UTC 09 Jul 2014	1300 UTC 09 Jul 2015	365		
				A3L	1790	0900 UTC 09 Jul 2014	1100 UTC 09 Jul 2015	365		
YUC10	21°50.360′N	84°59.841′W	608	LR75DW	122	0900 UTC 09 Jul 2014	1600 UTC 09 Jul 2015	365	25	16
				WH300UP	122	0900 UTC 09 Jul 2014	1500 UTC 09 Jul 2015	365	14	8
				SBE56	601	1100 UTC 09 Jul 2014	1400 UTC 09 Jul 2015	365		
Recovery Cruise CNK39										
YUC1	21°30.228′N	86°44.137′W	21	AQPUP	20	1900 UTC 07 Jul 2015	1600 UTC 09 Aug 2016	398	16	1
YUC2	21°32.356′N	86°30.326′W	62	WH300UP	50	1700 UTC 07 Jul 2015	2100 UTC 08 Aug 2016	398	11	4
YUC3	21°33.260′N	86°27.115′W	114	WH300UP	106	1600 UTC 07 Jul 2015	2100 UTC 08 Aug 2016	398	11	8
YUC4	21°34.412′N	86°21.291′W	505	LR75UP	489	1400 UTC 07 Jul 2015	1900 UTC 08 Aug 2016	398	54	8
YUC5	21°36.805′N	86°14.116′W	1149	LR75UP	500	0900 UTC 07 Jul 2015	1600 UTC 08 Aug 2016	398	49	8
				A3L	603	0900 UTC 07 Jul 2015	2200 UTC 24 Jul 2016	398		
				AaRCM11	724	0900 UTC 07 Jul 2015	1700 UTC 08 Aug 2016	398		
				SBE56	724	1000 UTC 07 Jul 2015	1800 UTC 08 Aug 2016	398		
				A2L	982	0900 UTC 07 Jul 2015	1900 UTC 08 Aug 2016	383		
				AaRCM11	1083	0800 UTC 07 Jul 2015	1700 UTC 08 Aug 2016	398		
				SBE56	1083	1000 UTC 07 Jul 2015	1500 UTC 08 Aug 2016	398		

TABLE 1. (Continued)

Mooring	Latitude	Longitude	Water depth (m)	Instrument	Instrument depth (m)	Start	End	Length of series (days)	No. of bins	Bin size (m)
YUC6	21°40.139'N	85°58.619'W	1890	AaSg	1190	1000 UTC 07 Jul 2015	1500 UTC 08 Aug 2016	398		
				LR75DW	102	0600 UTC 07 Jul 2015	0300 UTC 01 Dec 2015	146	35	16
				WH300UP	102	0600 UTC 07 Jul 2015	2000 UTC 07 Aug 2016	397	11	8
				SBE56	102	0600 UTC 07 Jul 2015	2000 UTC 07 Aug 2016	397		
				WH300UP	751	0600 UTC 07 Jul 2015	0400 UTC 29 Jul 2016	397	14	8
				A2L	758	0600 UTC 07 Jul 2015	1900 UTC 26 Jul 2016	387		
				SBE56	758	0600 UTC 07 Jul 2015	2100 UTC 07 Aug 2016	397		
				AaRCM11	866	0600 UTC 07 Jul 2015	2100 UTC 07 Aug 2016	397		
				A2L	1069	0500 UTC 07 Jul 2015	2100 UTC 07 Aug 2016	385		
				SBE56	1069	0600 UTC 07 Jul 2015	2200 UTC 07 Aug 2016	397		
				AaRCM11	1277	0500 UTC 07 Jul 2015	0900 UTC 05 Aug 2016	397		
				SBE56	1277	0800 UTC 07 Jul 2015	1900 UTC 07 Aug 2016	397		
				A3L	1580	0800 UTC 07 Jul 2015	1900 UTC 07 Aug 2016	397		
				AaSg	1732	0800 UTC 07 Jul 2015	1900 UTC 07 Aug 2016	395		
				SCT	1889	0800 UTC 07 Jul 2015	1900 UTC 07 Aug 2016	397		
				A3L	1890	0600 UTC 07 Jul 2015	2100 UTC 07 Aug 2016	397		
YUC7	21°39.631'N	85°43.441'W	2034	LR75DW	83	2000 UTC 06 Jul 2015	1500 UTC 07 Aug 2016	397	35	16
				WH300UP	83	1900 UTC 06 Jul 2015	1500 UTC 07 Aug 2016	397	11	8
				SBE56	83	2000 UTC 06 Jul 2015	1700 UTC 07 Aug 2016	397		
				A2L	116	2000 UTC 06 Jul 2015	0800 UTC 24 Jul 2016	397		
				AaRCM11	706	2000 UTC 06 Jul 2015	1700 UTC 07 Aug 2016	397		
				SBE56	706	2000 UTC 06 Jul 2015	1700 UTC 07 Aug 2016	397		
				A2L	965	2100 UTC 06 Jul 2015	1700 UTC 07 Aug 2016	383		
				SBE56	965	2100 UTC 06 Jul 2015	1700 UTC 07 Aug 2016	397		
				AaRCM11	1168	1900 UTC 06 Jul 2015	1700 UTC 07 Aug 2016	397		
				SBE56	1168	2000 UTC 06 Jul 2015	1300 UTC 18 Jul 2015	397		
				A6L	1527	2200 UTC 06 Jul 2015	1400 UTC 07 Aug 2016	397		
				AaRCM11	1710	2200 UTC 06 Jul 2015	1400 UTC 07 Aug 2016	397		
				A6L	1912	2200 UTC 06 Jul 2015	1400 UTC 07 Aug 2016	397		
				AaSg	2019	2200 UTC 06 Jul 2015	1400 UTC 07 Aug 2016	11		
YUC8	21°41.852'N	85°31.028'W	1694	LR75DW	112	1500 UTC 09 Jul 2015	1700 UTC 08 Feb 2016	214	35	16
				WH300UP	112	1500 UTC 09 Jul 2015	1200 UTC 07 Aug 2016	394	13	8
				A2L	643	1500 UTC 09 Jul 2015	0200 UTC 29 Jul 2016	385		
				AaSg	902	1500 UTC 09 Jul 2015	1300 UTC 07 Aug 2016	394		
				A3L	1160	1400 UTC 09 Jul 2015	1300 UTC 07 Aug 2016	394		
				AaSg	1412	1500 UTC 09 Jul 2015	1300 UTC 07 Aug 2016	394		
				AaSg	1670	1500 UTC 09 Jul 2015	1300 UTC 07 Aug 2016	394		
YUC9	21°44.926'N	85°14.629'W	1814	LR75DW	109	0100 UTC 10 Jul 2015	0900 UTC 07 Aug 2016	394	35	16
				WH300UP	109	0100 UTC 10 Jul 2015	0900 UTC 07 Aug 2016	394	13	8
				AaRCM11	738	0100 UTC 10 Jul 2015	0900 UTC 07 Aug 2016	394		
				SBE56	738	0200 UTC 10 Jul 2015	1000 UTC 07 Aug 2016	394		

TABLE 1. (*Continued*)

Mooring	Latitude	Longitude	Water depth (m)	Instrument	Instrument depth (m)	Start	End	Length of series (days)	No. of bins	Bin size (m)
				LR75DW	1091	0200 UTC 10 Jul 2015	1000 UTC 07 Aug 2016	394	18	16
				A3L	1582	0100 UTC 10 Jul 2015	1000 UTC 07 Aug 2016	394		
				AaSg	1790	0300 UTC 10 Jul 2015	0800 UTC 07 Aug 2016	394		
YUC10	21°50.415′N	84°59.812′W	609	LR75DW	122	2100 UTC 09 Jul 2015	1700 UTC 11 Aug 2016	398	26	16
				WH300UP	122	2000 UTC 14 Jul 2015	2100 UTC 22 Jul 2015	8	14	8
				A2L	601	2000 UTC 09 Jul 2015	0000 UTC 10 Jul 2016	366		

position [the horizontal position is not considered to vary, but the vertical position (depth) of the observation point is calculated based on the known vertical positions]. The iteration's mean field is sampled at these positions and appropriate current anomalies are then calculated and objectively interpolated with the chosen horizontal and vertical scales into a regular grid with a resolution of 0.05° in the horizontal and 20 m in the vertical for both the Yucatan and Florida sections. These resolutions provide a section with 2101 regular cells in Yucatan and 1081 in the Florida sections. The full set of hourly-interpolated maps provides an updated mean map that substitutes the initial reference map and the mapping process is repeated. The procedure converges quite rapidly, after a few (~5) iterations, reaching a mean map with nearly null update, therefore producing a "stable" mean current field consistent with anomalies for the scales used. It is worth remembering that the mean field obtained is a function of the dataset (their quantity and distribution on the section) and of the scales (horizontal and vertical) used for the objective interpolation of the current anomalies.

Initial decorrelation scales were obtained based on the correlation between the current observations time series as a function of their vertical and horizontal separation. Fitting exponential functions one obtains (536 m, 51 km) for the (vertical, horizontal) scales in Yucatan, while in Florida one obtains (490 m, 26 km; these calculations are included in the online supplemental material). In both sections the spreading of the correlation values is such that other similar scales could by determined by fitting other functions. However, the proposed method of analysis described above is to explore different scales and from them chose which scale combination in each channel produces transport estimates that best conserve mass in the GoM. For both sections the space of scales explored were from 20 to 100 km with 10-km increments (20:10:100) for the horizontal scales and from 300 to 1000 m with 100-m increments (300:100:1000) for the vertical scales; therefore, 72 interpolation iteration procedures were performed in each section. Observation to signal error variance was assumed to be 10% in all interpolations on both channels. In the Florida section the mean transport obtained over these 72 scale combinations, for the 4 years, fluctuated from 27.3 to 27.9 Sv, however, in the Yucatan Channel it varied from 15.8 to 28.1 Sv. This high scale-dependent variability of the 4-yr mean transport in Yucatan is a consequence of the poor sampling of the currents below 800 m during the first three deployments as mentioned above. In the Florida section the mean maps obtained with different scales are very similar and consistent, however for the Yucatan section there are larger

variations. To choose the most appropriate interpolation for each section it was decided to compare their 4-yr mean transport and the very low-pass-filter (annual running mean) series between the 72 iterations in the two channels and seek those that guaranteed volume conservation as much as possible, since the Yucatan and Florida sections are the only two open boundaries of the GoM with the surrounding ocean and it is desirable if not mandatory that the flows through them should conserve mass. Based on this physical argument, the most consistent results between the transports measured at both channels corresponded to a (vertical, horizontal) scale combination of (700 m, 60 km) for Yucatan and (600 m, 80 km) for the Florida section. This is further explained when discussing Fig. 7 in the next section.

3. Results

The mean current structure obtained in the Yucatan Channel is dominated by the surface intensified Yucatan Current (YC) core flowing into the GoM, on the western side of the Channel, with maximum mean currents reaching $120 \, \text{cm} \, \text{s}^{-1}$ (Fig. 3a, left panel). Considering the $10 \, \text{cm} \, \text{s}^{-1}$ contour as a boundary for the YC, it is clear that it occupies more than three-fourths of the Channel's surface and extends to depths around 800 m up to the center of the Channel. On the Cuban side, there is the presence of an intense ($>20 \, \text{cm} \, \text{s}^{-1}$) surface counter-current extending to about 350-m depth and then a weak broad countercurrent at depth, between 600 and 1400 m. At depth, on the Yucatan side, there is a countercurrent flowing into the Caribbean centered at 1200 m with a relatively large maximum current of around $10 \, \text{cm} \, \text{s}^{-1}$, which might be a consequence of the interpolation procedure due to the poor sampling of the currents in this area of the section. Except for this relatively large magnitude of the deep Yucatan side counter current, in general, this description of the mean current structure in Yucatan is in agreement with previous measurements (Sheinbaum et al. 2002; Ochoa et al. 2003; Abascal et al. 2003; Athié et al. 2015) and also with numerical model simulations (Ezer et al. 2003; Candela et al. 2003; Cherubin et al. 2005; Lin et al. 2009). The standard deviation (STD) of the current is larger than the mean in most of the channel section, except in the western surface region occupied by the YC surface core (Fig. 3a, right panel). Both the eastern surface Cuban countercurrent and the currents below 800 m present a high degree of variability. In the Florida section the mean current structure is dominated by the presence of the Florida Current (FC) occupying the whole channel above 800-m depth and flowing toward the Atlantic, with a surface northward off-centered maximum $> 110 \, \text{cm} \, \text{s}^{-1}$

(Fig. 3b, left panel). The upward-sloping current's STD contours in the middle of the channel are indicative of a very stable FC core and, in general, of currents above 600-m depth. Mean current sections obtained from carefully contouring all of the mean values of the observed current series longer than 365 days in each section (Fig. 3c) are similar and have the same characteristics as the mean sections obtained by imposing the continuity restriction described above (Figs. 3a,b, left panels). It is worth mentioning that the maximum yearly mean current observed at the surface on the Florida section is $115 \, \text{cm} \, \text{s}^{-1}$ (Fig. 3c, right panel). Leaman et al. (1987) analyzed data from a different section in the Florida Strait at 27°N, between Florida and the Bahamas, and observed a maximum surface mean current of $180 \, \text{cm} \, \text{s}^{-1}$. In understanding this relatively large discrepancy of maximum mean surface current between these two sections in the Florida Straits, two aspects are to be considered:

1) The section at 27°N has a maximum depth of less than 800 m and the width at the surface is 80 km; the section discussed in this article has a maximum depth of 1400 m and a width of 130 km at the surface.
2) Also, as further discussed in section 4, the section at 27°N has additional flow contributions from the Old Bahama and Northwest Providence Channels.

An important consideration in understanding the GoM throughflow is the restriction imposed by the shallowest sill in the system that corresponds to the ~800-m depth of the Bimini section at around the latitude of Miami (Niiler and Richardson 1973). This implies that in the Yucatan (Fig. 3a) and Florida (Fig. 3b) sections the throughflow is mainly related to the contribution above 800 m (or about the 6°C isotherm), with flows below this depth necessarily averaging out to zero transport in the two sections.

Time series of the calculated hourly transports in each Channel are shown in (Fig. 4). Although both have a mean of 27.6 Sv for this 4-yr period, the transport's STD is twice as large in Yucatan (11.4 Sv) than in Florida (5.7 Sv), with the hourly transport in Yucatan presenting even reversals as large as 10 Sv into the Caribbean. The tidal contribution to these transport time series has a strong diurnal character in Yucatan, with a tidal index (TI) = 8.2 [where TI is the ratio of tidal transport amplitudes of the 4 main diurnal to the 4 main semidiurnal constituents, i.e., $(Q_1 + O_1 + P_1 + K_1)/(N_2 + M_2 + S_2 + K_2)$], while in the Florida section it has a more mixed character (TI = 1.4). The strong diurnal character of the exchange through the Yucatan Channel is likely related to the excitation of a gravitational barotropic normal mode between the GoM and the Caribbean Sea, with a node in the Yucatan Channel, that has a period close to diurnal (~27 h).

TABLE 2. As in Table 1, but for the moorings deployed across the Florida Channel Section in the four deployments (CNK29, CNK34, CNK37 and CNK39) described in the text.

Mooring	Latitude	Longitude	Water depth (m)	Instrument	Instrument depth (m)	Start	End	Length of series (days)	No. of bins	Bin size (m)
Recovery Cruise CNK29										
EFL1	23°18.844'N	81°6.910'W	429	LR75DW	130	0400 UTC 08 Jul 2012	1400 UTC 26 Jun 2013	353	16	16
				WH300UP	130	0400 UTC 08 Jul 2012	1400 UTC 26 Jun 2013	353	12	8
				A3L	421	0500 UTC 08 Jul 2012	1400 UTC 26 Jun 2013	353		
EFL2	23°29.517'N	81°9.206'W	1316	LR75DW	130	0600 UTC 08 Jul 2012	1600 UTC 26 Jun 2013	353	33	16
				WH300UP	130	0600 UTC 08 Jul 2012	1600 UTC 26 Jun 2013	353	14	8
				LR75DW	704	0600 UTC 08 Jul 2012	0800 UTC 24 Nov 2012	139	24	16
EFL3	23°40.294'N	81°12.425'W	1377	LR75DW	131	0800 UTC 08 Jul 2012	1900 UTC 26 Jun 2013	353	34	16
				WH300UP	131	0800 UTC 08 Jul 2012	1800 UTC 26 Jun 2013	353	14	8
				LR75DW	728	0700 UTC 08 Jul 2012	1900 UTC 26 Jun 2013	353	25	16
				A3L	779	0900 UTC 08 Jul 2012	1900 UTC 26 Jun 2013	353		
EFL4	23°50.075'N	81°14.534'W	1335	LR75DW	144	0900 UTC 08 Jul 2012	2100 UTC 26 Jun 2013	353	33	16
				WH300UP	144	0900 UTC 08 Jul 2012	2000 UTC 26 Jun 2013	353	14	8
				LR75DW	734	0900 UTC 08 Jul 2012	2100 UTC 26 Jun 2013	353	23	16
EFL5	24°1.290'N	81°17.393'W	1030	LR75DW	130	1000 UTC 08 Jul 2012	1400 UTC 27 Jun 2013	354	32	16
				WH300UP	130	1100 UTC 08 Jul 2012	1400 UTC 27 Jun 2013	354	14	8
				LR75DW	574	1100 UTC 08 Jul 2012	1300 UTC 27 Jun 2013	354	21	16
				A3L	1020	1200 UTC 08 Jul 2012	1400 UTC 27 Jun 2013	354		
EFL6	24°13.129'N	81°21.062'W	576	LR75DW	130	1200 UTC 08 Jul 2012	1200 UTC 27 Jun 2013	354	25	16
				WH300UP	130	1200 UTC 08 Jul 2012	1200 UTC 27 Jun 2013	354	14	8
EFL7	24°24.117'N	81°23.937'W	180	WH300UP	130	1300 UTC 08 Jul 2012	1000 UTC 27 Jun 2013	353	13	8
				A6L	171	1400 UTC 08 Jul 2012	1000 UTC 27 Jun 2013	353		
Recovery Cruise CNK34										
EFL1	23°18.862'N	81°6.268'W	435	LR75DW	130	0400 UTC 27 Jun 2013	0900 UTC 12 Jul 2014	380	16	16
				WH300UP	130	0500 UTC 27 Jun 2013	1000 UTC 12 Jul 2014	380	10	8
				A3L	421	0600 UTC 27 Jun 2013	1000 UTC 12 Jul 2014	380		
EFL2	23°29.519'N	81°9.234'W	1316	LR75DW	130	0600 UTC 27 Jun 2013	1100 UTC 12 Jul 2014	380	36	16
				WH300UP	130	0600 UTC 27 Jun 2013	1200 UTC 12 Jul 2014	380	15	8
				LR75DW	704	0600 UTC 27 Jun 2013	1100 UTC 12 Jul 2014	380	30	16
EFL3	23°40.281'N	81°12.458'W	1372	LR75DW	131	2000 UTC 27 Jun 2013	1400 UTC 12 Jul 2014	379	36	16
				WH300UP	131	2000 UTC 27 Jun 2013	1300 UTC 12 Jul 2014	379	14	8
				LR75DW	779	2000 UTC 27 Jun 2013	1400 UTC 12 Jul 2014	379	26	16
EFL4	23°50.148'N	81°14.413'W	1335	LR75DW	130	2200 UTC 27 Jun 2013	2000 UTC 10 Jul 2014	377	34	16
				WH300UP	130	2200 UTC 27 Jun 2013	2000 UTC 10 Jul 2014	377	14	8
				LR75DW	734	2200 UTC 27 Jun 2013	2000 UTC 10 Jul 2014	377	28	16
EFL5	24°1.628'N	81°17.173'W	1025	LR75DW	129	0000 UTC 28 Jun 2013	1600 UTC 10 Jul 2014	377	36	16
				WH300UP	129	0000 UTC 28 Jun 2013	1600 UTC 10 Jul 2014	377	12	8
				LR75DW	574	0000 UTC 28 Jun 2013	1700 UTC 10 Jul 2014	377	23	16
				A6L	1020	0100 UTC 28 Jun 2013	1600 UTC 10 Jul 2014	377		

TABLE 2. (*Continued*)

Mooring	Latitude	Longitude	Water depth (m)	Instrument	Instrument depth (m)	Start	End	Length of series (days)	No. of bins	Bin size (m)
EFL6	24°13.138′N	81°21.986′W	564	LR75DW	130	0100 UTC 28 Jun 2013	1300 UTC 10 Jul 2014	377	23	16
				WH300UP	130	0100 UTC 28 Jun 2013	1400 UTC 10 Jul 2014	377	12	8
EFL7	24°24.140′N	81°23.803′W	180	WH300UP	130	0200 UTC 28 Jun 2013	1100 UTC 10 Jul 2014	377	13	8
				A2L	171	0400 UTC 28 Jun 2013	1200 UTC 10 Jul 2014	377		
Recovery Cruise CNK37										
EFL1	23°18.823′N	81°6.490′W	439	LR75DW	130	2200 UTC 12 Jul 2014	1100 UTC 12 Jul 2015	364	15	16
				SBE56	130	0000 UTC 13 Jul 2014	1000 UTC 11 Jul 2015	364		
				AaRCM1	421	0100 UTC 13 Jul 2014	1000 UTC 12 Jul 2015	363		
				SBE56	421	0100 UTC 13 Jul 2014	1000 UTC 12 Jul 2015	364		
EFL2	23°29.528′N	81°9.260′W	1314	LR75DW	129	2100 UTC 12 Jul 2014	1200 UTC 12 Jul 2015	364	35	16
				WH300UP	129	2100 UTC 12 Jul 2014	1300 UTC 12 Jul 2015	364	14	8
				SBE56	129	2100 UTC 12 Jul 2014	1300 UTC 12 Jul 2015	364		
				LR75DW	703	2200 UTC 12 Jul 2014	1300 UTC 12 Jul 2015	364	32	16
				SBE56	703	0000 UTC 13 Jul 2014	1100 UTC 12 Jul 2015	364		
				A2L	1290	2300 UTC 12 Jul 2014	1100 UTC 12 Jul 2015	364		
				SBE56	1290	2300 UTC 12 Jul 2014	1100 UTC 12 Jul 2015	364		
EFL3	23°40.260′N	81°12.472′W	1364	LR75DW	132	1900 UTC 12 Jul 2014	1200 UTC 13 Jul 2015	365	35	16
				WH300UP	132	1900 UTC 12 Jul 2014	1200 UTC 13 Jul 2015	365	14	8
				SBE56	132	1900 UTC 12 Jul 2014	1200 UTC 13 Jul 2015	365		
				A2L	727	1900 UTC 12 Jul 2014	1200 UTC 13 Jul 2015	365		
				SBE56	727	1900 UTC 12 Jul 2014	1200 UTC 13 Jul 2015	365		
				LR75DW	778	2100 UTC 12 Jul 2014	1000 UTC 13 Jul 2015	365	26	16
				SBE56	778	2100 UTC 12 Jul 2014	1000 UTC 13 Jul 2015	365		
				AaSg	1360	2100 UTC 12 Jul 2014	1000 UTC 13 Jul 2015	365		
EFL4	23°49.541′N	81°14.119′W	1332	LR75DW	130	0300 UTC 11 Jul 2014	0900 UTC 13 Jul 2015	367	33	16
				WH300UP	130	0300 UTC 11 Jul 2014	0900 UTC 13 Jul 2015	367	14	8
				SBE56	130	0300 UTC 11 Jul 2014	0900 UTC 13 Jul 2015	367		
				LR75DW	734	0300 UTC 11 Jul 2014	0900 UTC 13 Jul 2015	367	25	16
				SBE56	734	0500 UTC 11 Jul 2014	0700 UTC 13 Jul 2015	367		
				A2L	1320	0500 UTC 11 Jul 2014	0700 UTC 13 Jul 2015	367		
				SBE56	1320	0500 UTC 11 Jul 2014	0700 UTC 13 Jul 2015	367		
EFL5	24°1.792′N	81°17.053′W	1026	LR75DW	130	2200 UTC 10 Jul 2014	1600 UTC 12 Jul 2015	366	31	16
				WH300UP	130	2200 UTC 10 Jul 2014	1600 UTC 12 Jul 2015	366	13	8
				SBE56	130	2200 UTC 10 Jul 2014	1700 UTC 12 Jul 2015	366		
				LR75DW	573	2300 UTC 10 Jul 2014	1700 UTC 12 Jul 2015	366	23	16
				SBE56	573	0000 UTC 11 Jul 2014	1500 UTC 12 Jul 2015	366		
				AaSg	1020	0000 UTC 11 Jul 2014	1500 UTC 12 Jul 2015	366		
EFL6	24°13.148′N	81°21.979′W	569	SBE56	571	2000 UTC 10 Jul 2014	2100 UTC 10 Jul 2015	365		
EFL7	24°24.127′N	81°23.811′W	180	WH300UP	130	1600 UTC 10 Jul 2014	1900 UTC 12 Jul 2015	367	13	8
				MCT	130	1600 UTC 10 Jul 2014	2000 UTC 12 Jul 2015	367		

JOURNAL OF PHYSICAL OCEANOGRAPHY

VOLUME 49

TABLE 2. (*Continued*)

Mooring	Latitude	Longitude	Water depth (m)	Instrument	Instrument depth (m)	Start	End	Length of series (days)	No. of bins	Bin size (m)
					Recovery Cruise CNK39					
EFL1	23°18.988′N	81°5.951′W	432	LR75DW	130	2100 UTC 13 Jul 2015	2000 UTC 18 Aug 2016	401	16	16
				WH300UP	130	2100 UTC 13 Jul 2015	2000 UTC 18 Aug 2016	401	14	8
				SBE56	130	2300 UTC 13 Jul 2015	1800 UTC 18 Aug 2016	401		
				SBE56	421	2300 UTC 13 Jul 2015	1800 UTC 18 Aug 2016	401		
EFL2	23°30.008′N	81°8.873′W	1313	LR75DW	102	1900 UTC 13 Jul 2015	2000 UTC 13 Aug 2016	397	35	16
				WH300UP	102	1900 UTC 13 Jul 2015	2000 UTC 13 Aug 2016	397	12	8
				LR75DW	702	1900 UTC 13 Jul 2015	2000 UTC 13 Aug 2016	397	27	16
				AaRCM11	1290	2000 UTC 13 Jul 2015	2200 UTC 13 Aug 2016	397		
				SBE56	1290	2100 UTC 13 Jul 2015	1900 UTC 13 Aug 2016	396		
EFL3	23°40.284′N	81°11.741′W	1368	LR75DW	99	1800 UTC 13 Jul 2015	1700 UTC 13 Aug 2016	396	36	16
				SBE56	99	1800 UTC 13 Jul 2015	1800 UTC 13 Aug 2016	396		
				AaRCM11	724	1700 UTC 13 Jul 2015	1800 UTC 13 Aug 2016	397		
				SBE56	724	1800 UTC 13 Jul 2015	1800 UTC 13 Aug 2016	396		
				LR75DW	777	1900 UTC 13 Jul 2015	1600 UTC 13 Aug 2016	397	24	16
				A3L	1360	1900 UTC 13 Jul 2015	1600 UTC 13 Aug 2016	397		
EFL4	23°50.047′N	81°14.562′W	1328	LR75DW	96	1400 UTC 13 Jul 2015	1500 UTC 13 Aug 2016	397	32	16
				WH300UP	96	1500 UTC 13 Jul 2015	1400 UTC 13 Aug 2016	397	11	8
				SBE56	96	1400 UTC 13 Jul 2015	1500 UTC 13 Aug 2016	396		
				LR75DW	732	1400 UTC 13 Jul 2015	1500 UTC 13 Aug 2016	396	26	16
				A3L	1320	1600 UTC 13 Jul 2015	1300 UTC 13 Aug 2016	397		
EFL5	24°1.391′N	81°17.619′W	1026	LR75DW	104	0300 UTC 13 Jul 2015	2100 UTC 12 Aug 2016	396	25	16
				WH300UP	104	0300 UTC 13 Jul 2015	2100 UTC 12 Aug 2016	396	9	8
				LR75DW	573	0300 UTC 13 Jul 2015	2100 UTC 12 Aug 2016	396	20	16
				SBE56	573	0300 UTC 13 Jul 2015	2100 UTC 12 Aug 2016	396		
				AaRCM11	1020	0600 UTC 13 Jul 2015	2000 UTC 12 Aug 2016	396		
				SBE56	1020	0600 UTC 13 Jul 2015	2000 UTC 12 Aug 2016	396		
EFL6	24°13.059′N	81°21.980′W	577	LR75UP	569	0100 UTC 13 Jul 2015	1100 UTC 13 Aug 2016	397	30	16
EFL7	24°24.111′N	81°23.776′W	176	WH300UP	130	0000 UTC 13 Jul 2015	0900 UTC 13 Aug 2016	397	13	8
				MCT	130	0100 UTC 13 Jul 2015	1000 UTC 13 Aug 2016	397		
				A3L	171	0000 UTC 13 Jul 2015	0900 UTC 13 Aug 2016	397		

Unauthenticated | Downloaded 08/20/22 05:32 PM UTC
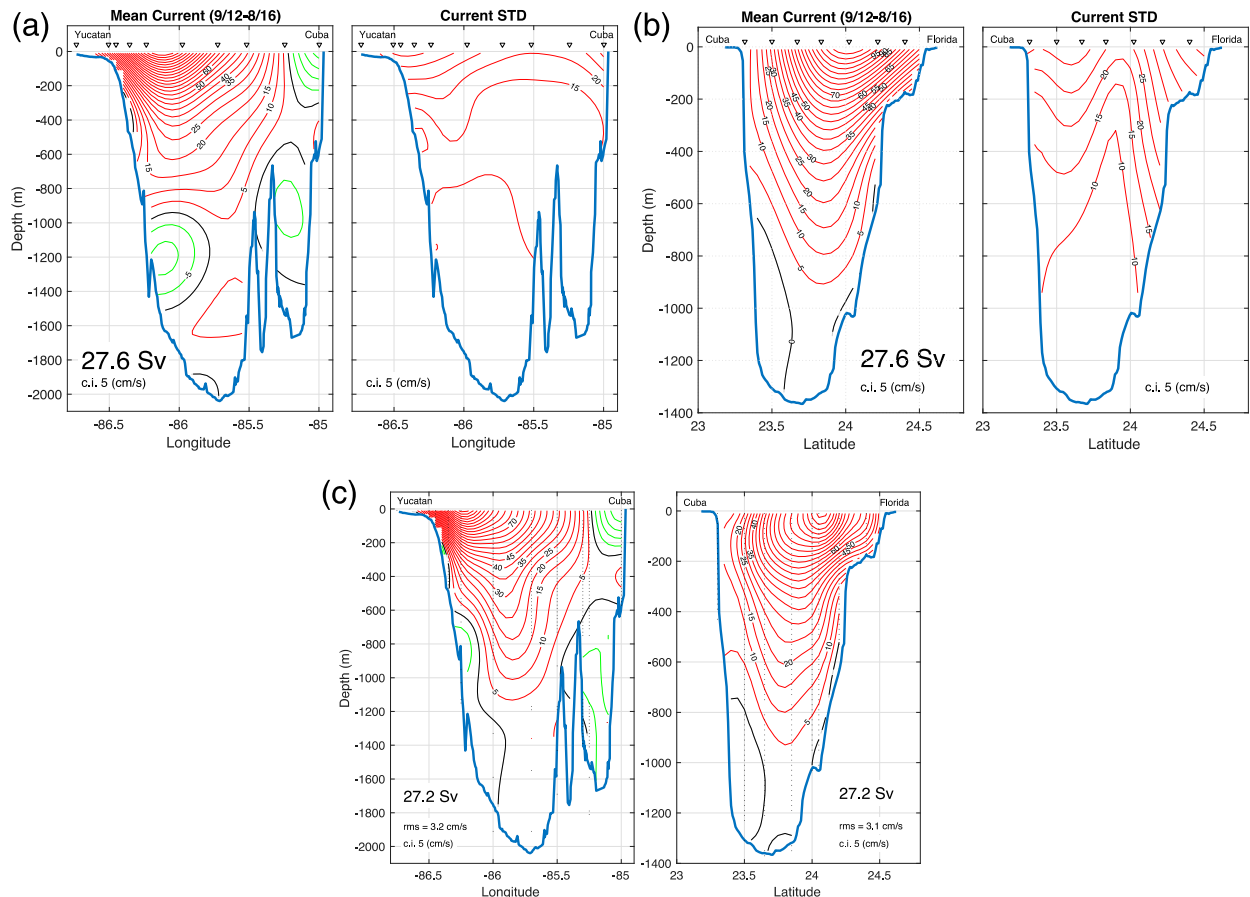
FIG. 3. (a) Four-year (September 2012–August 2016) (left) mean current and (right) current standard deviation in the Yucatan Channel. The mean section is obtained by the iterative method described in the text using the observed hourly data distribution and using a horizontal decorrelation scale of 60 km and a 700-m vertical decorrelation scale. Positive currents in red indicate currents into the Gulf of Mexico, negative currents in green are toward the Caribbean, and the zero contours are indicated in black. Contour interval (c.i.) magnitudes are indicated in the lower-left corner of each panel. The inverted triangles at the top indicate the mooring locations across the section. (b) Four-year (September 2012–August 2016) (left) mean current and (right) current standard deviation in the Florida Straits. The mean section is obtained by the iterative method described in the text using the observed hourly data distribution and using a horizontal decorrelation scale of 80 km and a 600-m vertical decorrelation scale. Positive currents (red contours) indicate flow out of the Gulf of Mexico. Contour interval magnitudes are indicated in the lower part of each panel. The inverted triangles at the top indicate the mooring locations across the section. (c) Mean current in (left) Yucatan and (right) Florida sections obtained from interpolation of mean currents at locations with more than 365 days of measuring period (small black dots) during the 4 years of observations. In the Yucatan section two extra points were added (marked with small red dots): a linear interpolation mean current at the center of the section (mooring 7) at 1390-m depth, and the extrapolation of the value measured at ~1280 m in mooring 9 toward the Cuban side to avoid unrealistic large extrapolation values on the Cuban deep side by the interpolation method. The contours follow the actual mean values very closely on both sections as indicated by the root-mean-square (rms) between the observed and interpolated values. The red contours indicate positive values, green contours indicate negative values, and black indicates the zero contours. Mean total transport, rms, and contour interval magnitude are indicated in the lower part of each panel.

This normal mode was calculated from a barotropic spectral model that superposes rotational and irrotational basis functions constructed over real bathymetry of the GoM–Caribbean Sea system. These basis functions are complemented with special island functions, to resolve the circulation around principal islands, and boundary functions to resolve the connections with the Atlantic Ocean (Sheinbaum et al. 1996). Another interesting feature about the observed exchange in each channel is that the harmonic synthesis of the transport series, without the annual and semiannual harmonics, can only explain 55% of the total transport variance at the Florida section, while at the Yucatan Channel the tidal synthesis can explain up to 82% of the observed transport variance. Certainly the less explained variance of the total transport in Florida has to do with the strong baroclinic tidal structure observed in this section, where the phase of the main diurnal tidal constituents of the
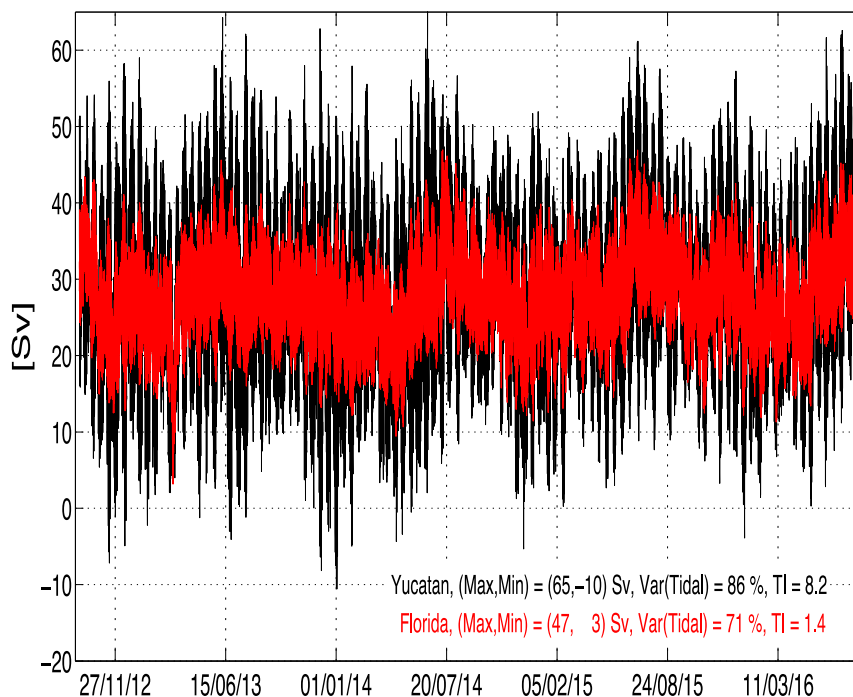
FIG. 4. Hourly time series of the total transport ($1\,\mathrm{Sv} = 10^6\,\mathrm{m^3\,s^{-1}}$) measured in the Yucatan Channel (black) and the Florida Straits (red). The maximum and minimum of each series is indicated as well as the total variance due to the astronomical tide contribution and the tidal index of each series.

along-channel currents tend to be 180° out of phase between being above or below 800-m depth. By contrast, the Yucatan diurnal tidal phases of the along-channel currents have a small and smooth transition from the surface to the bottom (Carrillo et al. 2007).

Applying a 7-day low-pass filter to the transport series reveals a very coherent behavior between the transports in the two channels (Fig. 5). Eliminating the high frequency ($>1/7$ days) mainly due to tides, the maximum and minimum transport, which varies between 12 and
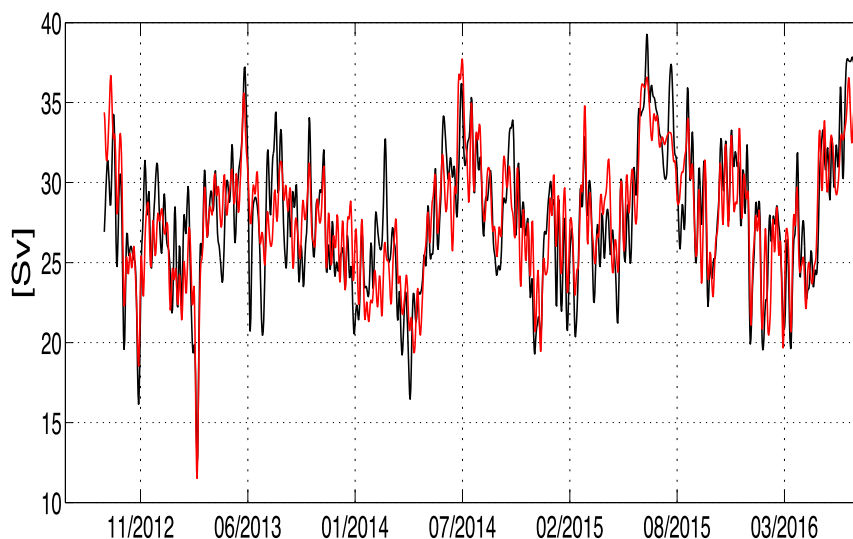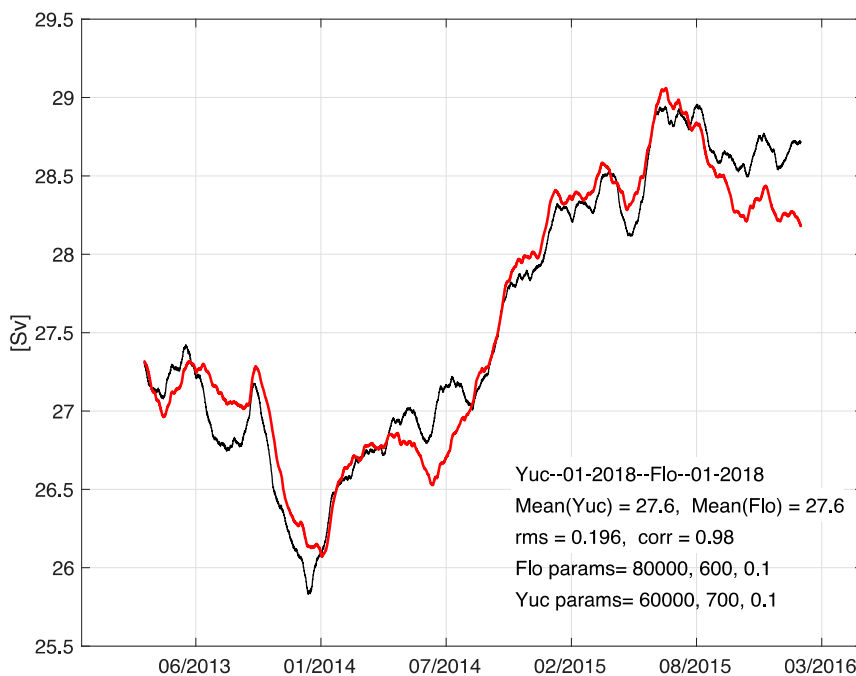

FIG. 5. Seven-day low pass of the transport measured in the Yucatan Channel (black) and the Florida Straits (red). The correlation between the filtered transport series is 0.83.
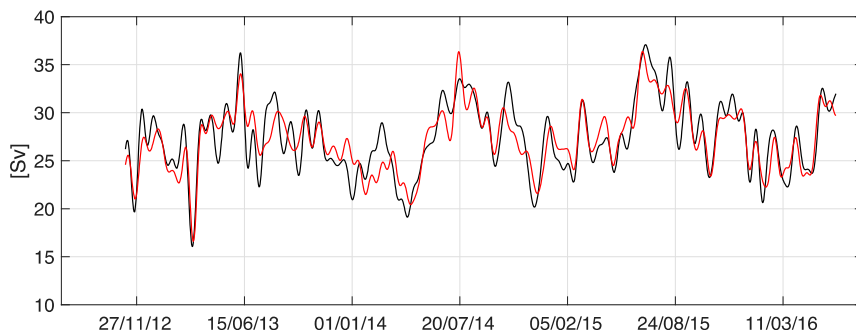
FIG. 6. Twenty-day low pass of the transport measured in the Yucatan Channel (black) and the Florida Straits (red). The correlation between the filtered transport series is 0.87.

39 Sv, is similar on both sections. The correlation between these two series is 0.83 with no appreciable lag, indicative of the simultaneousness of the processes affecting the transport at both channels. The 20-day low-pass-filtered transport series (Fig. 6) have a correlation of 0.87 and better reveal the presence of an appreciable seasonal cycle. The annual cycle over the 4 years has an amplitude of ~3.1 Sv (3.09 ± 0.62, 210° ± 12°, Florida; 3.14 ± 0.73, 211° ± 12°, Yucatan) with a maximum at the end of July and the semiannual signal an amplitude around 1 Sv (0.95 ± 0.58, 5° ± 35°, Florida; 1.33 ± 0.73, 16° ± 33°, Yucatan) with a maxima in January and July in accordance with previous reports (Niiler and Richardson 1973; Meinen et al. 2010; Athié et al. 2015; Athié et al. 2018, manuscript submitted to *J. Phys. Oceanogr.*).

The annual running mean (ARM) of the transport through Yucatan and Florida shows a 3-Sv range within the period analyzed. Figure 7 shows the ARM of the measured transport; each point on these plots is a yearly mean and therefore the seasonal or annual signal has been removed from the series. Strictly speaking, these two series should coincide, but this seems to be the best that can be done with the available data in the two channels, which, nonetheless, represent an unprecedented oceanographic effort. Even though the overall mean of both series is 27.6 Sv for the observed 4 years, the yearly mean varies ±1.5 Sv over this 4-yr period. This variability has to be imposed by a large-scale forcing outside of the GoM. A natural question arises, which is to what extent these low-frequency variations (periods longer than a year)

FIG. 7. ARM of observed transports in the Yucatan Channel (black) and in the Florida Straits. The correlation between the filtered transport series is 0.98.
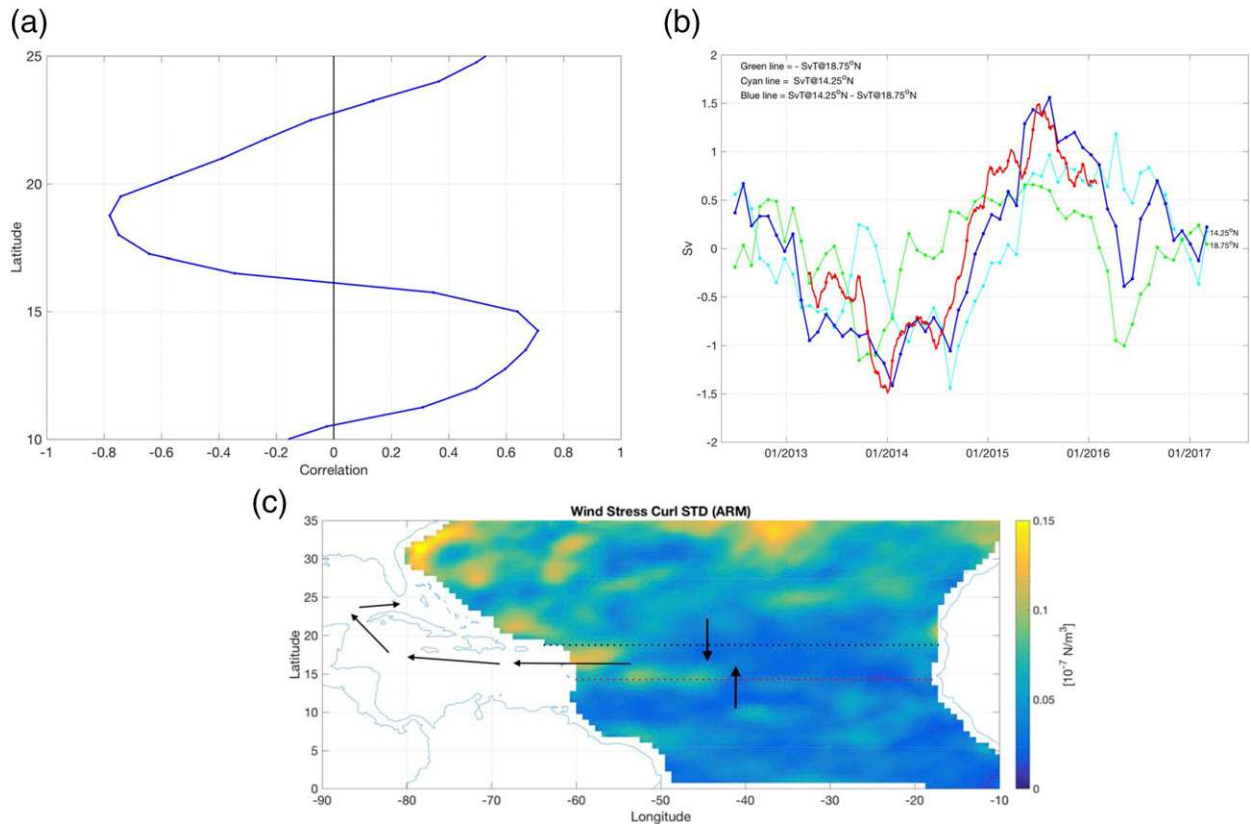
FIG. 8. (a) Correlation between the Sverdrup transport integrated zonally at different latitudes and the annual running mean transport in the Florida section. The correlations are calculated at zero lag with 35-month-long time series. (b) ARM Sverdrup transport (SvT) across 14.25°N (cyan line), SvT across 18.75°N (green line), their sum (blue line), and the ARM of the transport measured in the Florida Straits (red line) from Fig. 7. (c) Sketch of the convergence of the Sverdrup transport across 14.25° and 18.25°N and its flow into the Caribbean and the Gulf of Mexico. The background color map indicates the WSC standard deviation of the ARM-filtered WSC series from January 2012 to December 2017. The WSC is computed from the ERA-Interim wind database (Berrisford et al. 2011).

can be connected to the Sverdrup transport in the North Atlantic.

According to the Sverdrup balance, the meridional transport of the entire water column in the vast ocean interior, outside of the intense western boundary currents, is directly related and locally determined by the curl of the wind stress, that is,

$$V = \int_{-H}^{0} v\, dz = \frac{1}{\beta \rho_o} \mathrm{curl}(\boldsymbol{\tau}),$$

where V is the vertical integral of the meridional velocity v from the bottom of the ocean H to the surface, β is the northward spatial derivative of the Coriolis parameter, ρ_o is the average value of the seawater density, and $\boldsymbol{\tau}$ is the wind stress at the ocean surface (Pedlosky 1996).

Using the 6-hourly wind fields from ERA-Interim (Berrisford et al. 2011) for the North Atlantic, with a spatial resolution of 0.75°, the wind stress at every grid point is calculated and averaged monthly over the North

Atlantic Ocean. With these monthly wind stress averages, the wind stress curl is computed at every grid point using central difference approximations. The wind stress curl is then integrated zonally across the North Atlantic at all available latitudes from 5° to 30° and multiplied by $1/(\rho_o\beta)$ to obtain the zonally integrated Sverdrup transport as a function of latitude. The Sverdrup balance is a steady solution that, if anything, might apply to the very long period (more than a year) ocean circulation patterns. The monthly Sverdrup transport time series thus obtained are quite noisy and are smoothed by performing an ARM similar to the one applied to the transports measured in Florida and Yucatan. These smoothed Sverdrup transport series at each latitude are then correlated to the observed transport through Florida. It is interesting to notice that the correlation oscillates between positive and negative values from 0.71 at 14.25°N to −0.78 at 18.75°N (Fig. 8a). The high correlations of the zonally integrated Sverdrup transports across 14.25° and 18.75°N imply a convergence of the
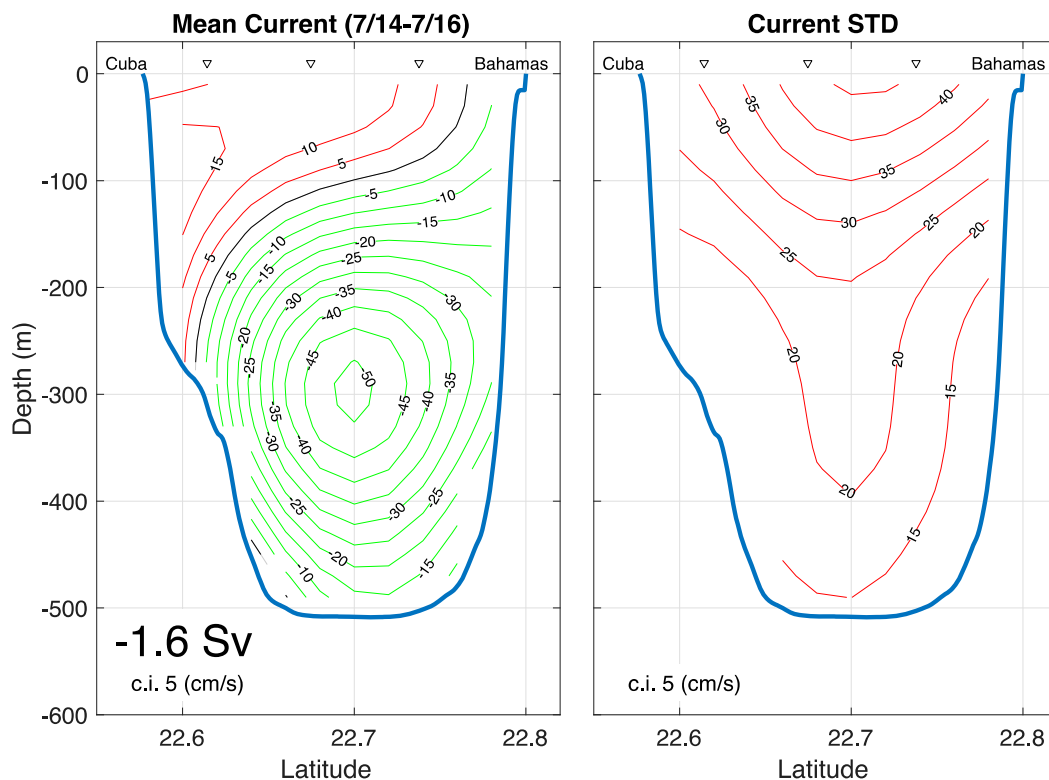
FIG. 9. Two-year (July 2014–July 2016) (left) mean current and (right) current standard deviation in the Old Bahama Channel section. The mean is obtained by the iterative method described in the text using the observed hourly data distribution and using a horizontal decorrelation scale of 15 km and a 300-m vertical scale. Negative current values (green contours) correspond to northwestward flow, i.e., toward the Florida Cable section. Contour interval magnitudes are indicated in the lower-left corner of each panel. The inverted triangles at the top indicate the mooring locations across the section.

Sverdrup transport across these latitudes that correlates very well with the observed ARM transport through the Florida section. Figure 8b shows the plot of the demeaned measured ARM transport in Florida and the demeaned ARM Sverdrup transport at 14.25° and 18.75°N; the amplitude of the variability is similar on the two series $\sim \pm 1$ Sv. The transport through 18.75°N is southward and part of the anticyclonic North Atlantic Subtropical Gyre, while the flow through 14.25°N is northward and part of the cyclonic North Atlantic Tropical Gyre (Mayer and Weisberg 1993). Considering these two contributions, the differential Sverdrup transport (blue line in Fig. 8b) is obtained, which has a correlation of 0.94 with the transport observed at the Florida section. These two transports imply a convergence between these latitudes and therefore a flow directed to the west into the Caribbean, the GoM, and out into the North Atlantic through the Florida section (Fig. 8c).

This interpretation may appear to contradict the theoretical result obtained by Anderson and Corry (1985), indicating that the nontopographic Sverdrup balance is unlikely to hold for the seasonal/annual cycle

observed at the cable section at 27°N, mainly because of the relatively slow westward propagation speed of the Rossby waves at this latitude. However, Figs. 7 and 8 relate to a lower-frequency response at periods longer than a year. By applying a yearly running mean filter, the seasonal/annual cycle is eliminated from the transport series; hence, Fig. 8b is addressing the ocean's lower-frequency response where the Sverdrup nontopographic balance seems to hold. The main point here is that two independent transport estimates are derived from different datasets and appear to be connected. Possible explanations are addressed in more depth in the discussion section below.

4. The flow through the Old Bahama Channel

Three moorings, each of them equipped with an upward-looking 75 kHz ADCP, were deployed across the Old Bahama Channel (~78.4°W; Fig. 1) for a 2-yr period (July 2014–July 2016). The hourly current observations were interpolated using the same optimal iterative procedure into a regular grid with a resolution
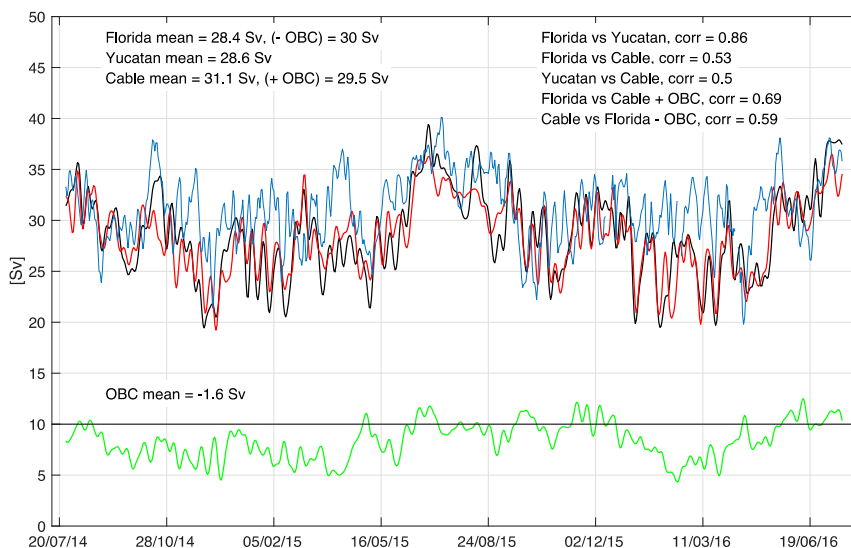
FIG. 10. Seven-day filtered time series of transport at Yucatan Channel (black), Florida Straits (red), Florida Cable section (blue, ~26.7°N) (Meinen et al. 2010), and at a section across Old Bahama Channel (green, ~22.8°N; +10 Sv for clarity, note that the transport is negative because at the Old Bahama section the mean flow is westward, i.e., toward the Florida Straits). For the location of these sections, see Fig. 1.

of 0.02° in the horizontal and 20 m in the vertical. This resolution provided 224 regular cells in the section. A direct decorrelation estimation with the measurements provided a horizontal scale of 15 km and a vertical scale of 300 m as the most appropriate to use in this section. The mean current structure presents a midchannel deep jet centered at around 290-m depth with a maximum mean current core around 50 cm s^{-1} (Fig. 9, left panel). This core is quite stable according to the current's STD (Fig. 9, right panel). The surface layer above 150 m is more variable and presents a weak mean current on the Cuban side flowing southeastward. The hourly transport time series (not shown) has a mean of 1.6 Sv toward the Straits of Florida, with a relatively large standard deviation of 1.9 Sv, a maximum of 6.9 Sv toward Florida, and a minimum southeastward transport of 3.9 Sv. Both the observed current structure, as well as the mean transport, are consistent with previous measurements made with a year-long time series from a four-current meter mooring located at the center of the channel in 1991 (Atkinson et al. 1995; Hamilton et al. 2005).

The simultaneously observed 7-day filtered transport time series in Yucatan Channel, the Florida Straits (~81°W), the Florida Cable section (~26.7°N), and a section across the Old Bahama Channel (~78.4°W) for these two years (July 2014–July 2016) are shown in Fig. 10. For this period the mean transport in Yucatan is 28.6 and 28.4 Sv in Florida; this discrepancy is well within the standard error of both means, while at the Florida Cable section and at the Old Bahama Channel mean northward

transports of 31.1 and 1.6 Sv, respectively, are observed. These numbers imply that the Northwest Providence Channel only contributes with 1.1 Sv to the mean transport observed at the Cable section during this 2-yr period. It is interesting that the correlation between the transport at the Florida section and that measured at the Cable section is low (0.53); however, if the transport measured at the Old Bahama section is added to the Cable section series, the correlation with the Florida section improves to 0.69.

5. Discussion

The differences observed in the low-pass time series of the computed transport through Yucatan Channel and the Florida Strait, specifically the differences in the 20-day low pass (Fig. 6) and ARM (Fig. 7), emphasize the difficulties of obtaining such estimates—a problem described in other channels or straits (Godin et al. 1981; Bryden et al. 1994). Furthermore, the high dispersion of transport estimates in the Yucatan Channel, based on the different vertical and horizontal scales explored in the interpolation, imply that the flow through Yucatan is much more complex than previously expected. A straightforward improvement might be the addition of observations in places where the current structure is poorly resolved, that is, in the deep Cuban and Yucatan sides of the channel. A major difficulty in the Yucatan section is the complex topography on the Cuban side, where several seamounts are present along, northward, and southward of the section.
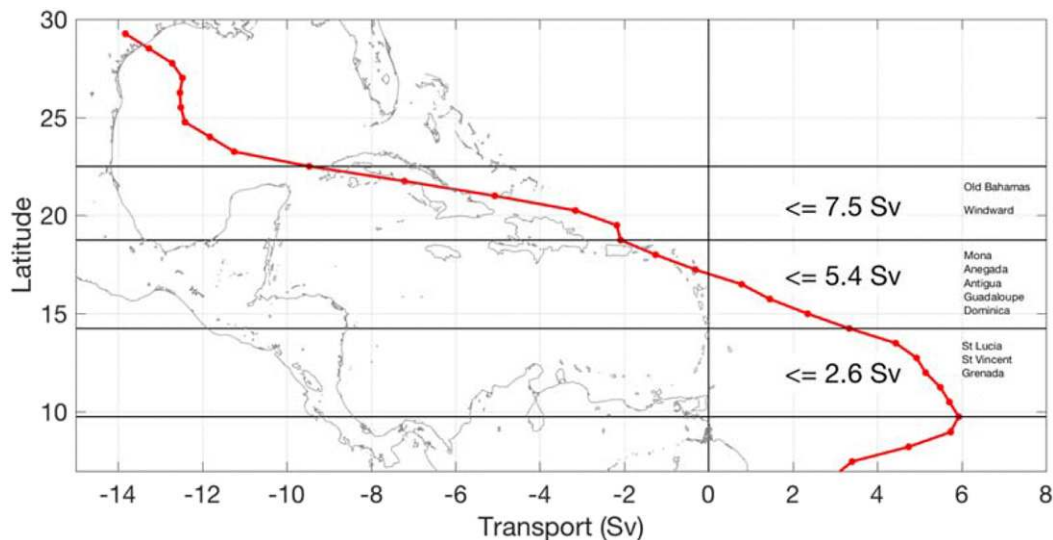
FIG. 11. Mean meridional Sverdrup transport vs latitude over the 4 years analyzed (July 2012–July 2016; red line). The arrows and numbers indicate the mean convergent Sverdrup transport that must exit to the west, either entering the Caribbean or feeding western boundary currents. The latitudes of these zonal boxes are at key limits suggested by previous studies of Caribbean inflows, i.e., windward and leeward island passages (Johns et al. 2002) and results present in this work. The name of the main Caribbean passages on the right are indicated at their approximate latitudes. The background map is for reference.

A thorough demonstration that the nontopographic Sverdrup balance is at work in the relation obtained in Fig. 8 is the subject of an ongoing study, but there are several arguments, described below, that support this as the most likely explanation. According to Anderson and Corry (1985) "the Sverdrup balance is unlikely to hold at annual period for the North Atlantic. For periods much less than the time taken for the wind-generated baroclinic Rossby waves to pass over bottom topography, the ocean response is primarily that for a homogeneous ocean and thus strongly modified by topography. For periods much longer than this time, the Rossby waves compensate for the effect of topography and the nontopographic Sverdrup balance holds." Baroclinic Rossby waves can be generated, at all latitudes, by seasonal (or lower frequency) wind fluctuations and the presence of boundaries or steep topography (Mid-Atlantic Ridge; Barnier 1988). At 27°N in the North Atlantic, the Mid-Atlantic Ridge is ~3000 km from the western boundary; at 16°N it is only 1600 km from the Lesser Antilles. Also, in the limit of long planetary waves, the phase (or group) speed (westward) of the (nondispersive) baroclinic Rossby waves is a function of latitude (Gill 1982, p. 503): at 27°N it is ~4 cm s^{-1}, while at 16°N it is ~14 cm s^{-1}, for the first baroclinic mode. This would imply that baroclinic Rossby waves generated at the Mid-Atlantic Ridge take ~870 days to reach the western boundary at 27°N and only ~130 days to reach the Lesser Antilles channels entering the Caribbean at ~16°N. Additionally, there is direct observed evidence

that in reality planetary long waves propagate faster than linear theory predicts, increasing with latitude from a factor of 1.5 times faster in the tropics up to 4 times faster in the subpolar oceans (DiNezio et al. 2009). Since Fig. 8b is related to variability at periods longer than annual, it seems that baroclinic Rossby waves at the latitudes ~16°N might have enough time to travel to the western boundary and mask the topographic effects to permit the nontopographic Sverdrup balance to hold there. The argument supporting Fig. 8b is that at interannual periods the Sverdrup transport convergence enters the Caribbean through the Lesser Antilles passages, mainly between 14° and 18°N, responding to a nontopographic Sverdrup balance, because at these latitudes the baroclinic Rossby waves generated by the wind variability at interannual periods have enough time to arrive at the western boundary and compensate for the effects of topography and this is reflected in the interannual variability observed in the Yucatan and Florida flows in the GoM. Apart from the arguments given above, Fig. 8c shows the wind stress curl (WSC) standard deviation of the ARM filtered WSC series from January 2012 to December 2017. It is evident that the largest variability of the interannual WSC signal occurs close to the Antilles between 14° and 18°N. Since baroclinic Rossby waves can be exited anywhere there is a significant WSC variation, it is plausible that they are being generated fairly close to the Antilles, thus permitting the nontopographic Sverdrup balance to hold and the related transport to enter the Caribbean there.

According to Johns et al. (2002), the observed transport into the Caribbean through the Windward Islands Passages (composed of the Grenada, St. Vincent, and St. Lucia Passages) is 10.1 ± 2.4 Sv, through the Leeward Islands Passages (Dominica, Guadeloupe, Antigua, and Anegada Passages) is 8.3 ± 2.3 Sv, and through the two passages of the Greater Antilles, Mona and Windward, are 3.0 and 7.0 Sv, respectively. These would roughly add up to a climatological average of 28 Sv entering the GoM through Yucatan Channel. This total transport is expected to be the sum of the wind-forced Sverdrup transport component and that due to the MOC component, both of which are expected to contribute in about equal parts to the total transport (Schmitz and McCartney 1993; Johns et al. 2002). From their wind-forced model simulations, driven by Hellerman and Rosenstein (1983) monthly winds, Johns et al. (2002) obtained a total Caribbean inflow of 17.2 Sv from winds only, and 28.3 Sv using both winds and MOC contributions (values obtained from their Fig. 5). These estimates imply a MOC climatological contribution to the GoM throughflow of around 11.1 Sv. For the 4-yr period (September 2012–August 2016), using the ERA-Interim winds, a total Caribbean inflow of 13.8 Sv is obtained, considering the Sverdrup transport convergence in the Atlantic between the latitudes of 9.75° and 22.5°N using the ERA-Interim winds (Fig. 11). This would imply, given the 27.6 Sv total, that the mean MOC and the wind-driven circulation contribute equally to the flow through the GoM during this period (~13.8 Sv).

The fact that there is such a good correlation between the ARM transport in the Florida section and that resulting from the Sverdrup transport convergence across 14.25° and 18.75°N for this specific 4-yr period might be fortuitous, in the sense that for other time periods the transport reflected in Florida might come from the Sverdrup contribution from different latitudes and/or entering the system through different passages in the Lesser and/or Greater Antilles. This correlation also implies that the MOC contribution to the throughflow at interannual scales was basically constant during this 4-yr period, a conjecture supported by new observations of the Atlantic meridional overturning cell (AMOC) at 26°N (Smeed et al. 2018).

6. Conclusions

Simultaneous transport measurements in Yucatan Channel, Straits of Florida (between Cuba and the Florida Keys), and the Cable section between Florida and the Bahamas, imply an important contribution (~2.7 Sv, on average) of flows outside the GoM to the overall transport of the Florida Current. Also, the transport variability observed at the Cable section differs to that observed at the Florida section (~81°W) due to the contributions from the Old Bahama and Northwest Providence Channels, with the former presenting a transport standard deviation of 1.9 Sv during the 2-yr measuring period discussed here. This implies that using the flow measured at the Cable section as representative of the Loop Current flow out of the GoM might be misleading, a proposition supported by previous work (Hamilton et al. 2005).

The observations reported here indicate that the interannual variability observed in the Florida Straits can be related to changes in the Sverdrup transport convergence between the latitudes of 14.25° and 18.75°N, for the 4-yr period analyzed. The contribution of this convergence to the observed mean throughflow of 27.6 Sv is only 5.4 Sv. However, there are potentially 2.6 Sv entering between the latitudes of 9.75° and 14.5°N and 7.5 Sv between the latitudes of 18.75° and 22.5°N during the period analyzed (Fig. 11). A conjecture also supported by the presence of high WSC variability close to the western boundary between these latitudes (Fig. 8c). This would imply a net inward mean transport of 5.9 Sv through the Windward Passage, assuming that 1.6 Sv flows northward through the Old Bahama Channel outside the Gulf of Mexico–Caribbean Sea system (Fig. 11). These three contributions, that is, 5.9, 5.4, and 2.6 Sv, add up to 13.9 Sv that would be the wind-driven mean transport flowing into the GoM through Yucatan Channel, implying an approximate equal mean MOC contribution of around 13.7 Sv flowing through the GoM during this 4-yr period.

REFERENCES

Abascal, A. J., J. Sheinbaum, J. Candela, J. Ochoa, and A. Badan, 2003: Analysis of flow variability in the Yucatan Channel. *J. Geophys. Res.*, **108**, 3381, https://doi.org/10.1029/2003JC001922.

Anderson, D. L. T., and R. A. Corry, 1985: Seasonal transport variations in the Florida Straits: A model study. *J. Phys. Oceanogr.*, **15**, 773–786, https://doi.org/10.1175/1520-0485(1985)015<0773:STVITF>2.0.CO;2.

Athié, G., J. Sheinbaum, R. Leben, J. Ochoa, M. R. Shannon, and J. Candela, 2015: Interannual variability in the Yucatan

Channel flow. *Geophys. Res. Lett.*, **42**, 1496–1503, https://doi.org/10.1002/2014GL062674.

Atkinson, L. P., T. Berger, P. Hamilton, E. Waddell, K. Leaman, and T. N. Lee, 1995: Current meter observations in the Old Bahamas Channel. *J. Geophys. Res.*, **100**, 8555–8560, https://doi.org/10.1029/95JC00586.

Barnier, B., 1988: A numerical study on the influence of the mid-Atlantic Ridge on nonlinear first-mode baroclinic Rossby waves generated by seasonal winds. *J. Phys. Oceanogr.*, **18**, 417–433, https://doi.org/10.1175/1520-0485(1988)018<0417:ANSOTI>2.0.CO;2.

Berrisford, P., and Coauthors, 2011: The ERA-Interim Archive: Version 2.0. ERA Rep. Series 1, 23 pp., https://www.ecmwf.int/sites/default/files/elibrary/2011/8174-era-interim-archive-version-20.pdf.

Bretherton, F. P., R. E. Davis, and C. B. Fandry, 1976: A technique for objective analysis and design of oceanographic experiments applied to MODE-73. *Deep-Sea Res. Oceanogr. Abstr.*, **23**, 559–582, https://doi.org/10.1016/0011-7471(76)90001-2.

Bryden, H. L., J. Candela, and T. H. Kinder, 1994: Exchange through the Strait of Gibraltar. *Prog. Oceanogr.*, **33**, 201–248, https://doi.org/10.1016/0079-6611(94)90028-0.

Candela, J., S. Tanahara, M. Crepon, B. Barnier, and J. Sheinbaum, 2003: Yucatán Channel flow: Observations versus CLIPPER ATL6 and MERCATOR PAM models. *J. Geophys. Res.*, **108**, 3385, https://doi.org/10.1029/2003JC001961.

Carrillo, F., J. Ochoa, J. Candela, A. Badan, J. Sheinbaum, and I. Gonzalez, 2007: Tidal currents in the Yucatan Channel. *Geofis. Int.*, **46** (3), 199–209.

Cherubin, L. M., W. Sturges, and E. P. Chassignet, 2005: Deep flow variability in the vicinity of the Yucatan Straits from a high-resolution numerical simulation. *J. Geophys. Res.*, **110**, C04009, https://doi.org/10.1029/2004JC002280.

DiNezio, P. N., L. J. Gramer, W. E. Johns, C. S. Meinen, and M. O. Baringer, 2009: Observed interannual variability of the Florida Current: Wind forcing and the North Atlantic Oscillation. *J. Phys. Oceanogr.*, **39**, 721–736, https://doi.org/10.1175/2008JPO4001.1.

Ezer, T., L.-Y. Oey, W. Sturges, and H.-C. Lee, 2003: The variability of currents in the Yucatan Channel: Analysis of results from a numerical ocean model. *J. Geophys. Res.*, **108**, 3012, https://doi.org/10.1029/2002JC001509.

Gill, A. E., 1982: *Atmosphere-Ocean Dynamics*. Academic Press, 662 pp.

Godin, G., J. Candela, and R. de la Paz-Vela, 1981: On the feasibility of detecting net transports in and out of Georgia Strait with an array of current meters. *Atmos.–Ocean*, **19**, 148–157, https://doi.org/10.1080/07055900.1981.9649106.

Hamilton, P., J. C. Larsen, K. D. Leaman, T. N. Lee, and E. Waddell, 2005: Transports through the Straits of Florida. *J. Phys. Oceanogr.*, **35**, 308–322, https://doi.org/10.1175/JPO-2688.1.

Hellerman, S., and M. Rosenstein, 1983: Normal monthly wind stress over the world ocean with error estimates. *J. Phys. Oceanogr.*, **13**,

1093–1104, https://doi.org/10.1175/1520-0485(1983)013<1093:NMWSOT>2.0.CO;2.

Johns, W. E., T. L. Townsend, D. M. Frantantoni, and W. D. Wilsion, 2002: On the Atlantic inflow to the Caribbean Sea. *Deep-Sea Res. I*, **49**, 211–243, https://doi.org/10.1016/S0967-0637(01)00041-3.

Leaman, K. D., R. L. Molinari, and P. S. Vertes, 1987: Structure and variability of the Florida Current at 27°N: April 1982–July 1984. *J. Phys. Oceanogr.*, **17**, 565–583, https://doi.org/10.1175/1520-0485(1987)017<0565:SAVOTF>2.0.CO;2.

Lin, Y., R. J. Greatbatch, and J. Sheng, 2009: A model study of the vertically integrated transport variability through the Yucatan Channel: Role of Loop Current evolution and flow compensation around Cuba. *J. Geophys. Res.*, **114**, C08003, https://doi.org/10.1029/2008JC005199.

Mayer, D. A., and R. H. Weisberg, 1993: A description of COADS surface meteorological fields and the implied Sverdrup transports for the Atlantic Ocean from 30°S to 60°N. *J. Phys. Oceanogr.*, **23**, 2201–2221, https://doi.org/10.1175/1520-0485(1993)023<2201:ADOCSM>2.0.CO;2.

Meinen, C. S., M. O. Baringer, and R. F. Garcia, 2010: Florida Current transport variability: An analysis of annual and longer-period signals. *Deep-Sea Res. I*, **57**, 835–846, https://doi.org/10.1016/j.dsr.2010.04.001.

Niiler, P. P., and W. S. Richardson, 1973: Seasonal variability of the Florida Current. *J. Mar. Res.*, **31**, 144–167.

Ochoa, J., A. Badan, J. Sheinbaum, and J. Candela, 2003: CANEK: Measuring transport in the Yucatan Channel. *Nonlinear Processes in Geophysical Fluid Dynamics*, O. U. Velasco Fuentes, J. Sheinbaum, and J. Ochoa, Eds., Kluwer Academic Publishers, 275–286, https://doi.org/10.1007/978-94-010-0074-1_16.

Pedlosky, J., 1996: *Ocean Circulation Theory*. Springer, 462 pp.

Roemmich, D., 1983: Optimal estimation of hydrographic station data and derived fields. *J. Phys. Oceanogr.*, **13**, 1544–1549, https://doi.org/10.1175/1520-0485(1983)013<1544:OEOHSD>2.0.CO;2.

Rousset, C., and L. M. Beal, 2011: On the seasonal variability of the currents in the Strait of Florida and Yucatan Channel. *J. Geophys. Res.*, **116**, C08004, https://doi.org/10.1029/2010JC006679.

Schmitz, W. J., Jr., and M. S. McCartney, 1993: On the North Atlantic circulation. *Rev. Geophys.*, **31**, 29–49, https://doi.org/10.1029/92RG02583.

Sheinbaum, J., J. Zavala, and J. Candela, 1996: Modelación numérica del Golfo de México y Mar Caribe. *Contribuciones a la Oceanografía Física en México*, M. F. Lavin, Ed., Monografía No. 3, Unión Geofísica Mexicana, 243–264.

——, J. Candela, A. Badan, and J. Ochoa, 2002: Flow structure and transport in Yucatan Channel. *Geophys. Res. Lett.*, **29**, 1040, https://doi.org/10.1029/2001GL013990.

Smeed, D. A., and Coauthors, 2018: The North Atlantic Ocean is in a state of reduced overturning. *Geophys. Res. Lett.*, **45**, 1527–1533, https://doi.org/10.1002/2017GL076350.